UDK 669.24:669.058.67
Original scientific article/Izvirni znanstveni članek

ISSN 1580-2949
MTAEC9, 58(2)217(2024)

INFLUENCE OF SPRAY DISTANCE ON THE POROSITY OF Ni-BASED AMORPHOUS COATINGS: NUMERICAL SIMULATION AND EXPERIMENT

VPLIV RAZDALJE NAPRŠEVANJA NA POROZNOST AMORFNE PREVLEKE NA OSNOVI NIKLJA: NUMERIČNA SIMULACIJA IN EKSPERIMENT

Rui Wang, Deming Wang, Nianchu Wu*

Liaoning Petrochemical University, School of Mechanical Engineering, Fushun 113001, P.R. China

Prejem rokopisa – received: 2023-09-20; sprejem za objavo – accepted for publication: 2024-02-27

doi:10.17222/mit.2023.1002

The influence of injection distance on the porosity of Ni-based amorphous coatings (AMCs) prepared with a high-velocity air fuel (HVAF) process is discussed based on a numerical analysis and experimental methods. A computational fluid dynamics model was established to demonstrate the gas flow field and behavior of particles in flight at different spraying distances during HVAF spraying. When analyzing the changes in the particle velocity and temperature, the spraying distance is less than 30 μm. The velocity and temperature changes of small particles have a significant impact, and the optimal spray distance (350 mm) for obtaining a low porosity coating is predicted. The calculation was validated experimentally by producing a Ni-based AMC with a low porosity (1.87 %) that was manufactured using the predicted HVAF optimal spraying distance.

Keywords: Ni-based amorphous coating, porosity, HVAF, computational simulation, spray distance

V članku je opisan vpliv razdalje napršev anja na poroznost amorfnih prevlek na osnovi niklja (Ni) izdelanih s postopkom zelo hitrega napršev anja v mešanici kurilnega plina (propana) in zraka (HVAF; angl.: high-velocity air fuel). Raziskavo so izvedli s pomočjo eksperimentalnih in numeričnih metod. Razvili so model temelječ na računalniški dinamiki fluidov (tekočin) zato, da so lahko predstavili polje pretakanja plinov in obnašanje delcev med njihovim letom proti podlagi pri različno izbranih razdaljah napršev anja s postopkom HVAF. Z simulacijami in analizami sprememb hitrosti ter temperature delcev so ugotovili, da je najmanjša možna razdalja napršev anja 30 μm. Spremembe hitrosti in temperature majhnih delcev delcev močno vplivajo na debelino prevleke. Ugotovili so, da je optimalna razdalja napršev anja 350 mm za izdelavo prevlek z majhno poroznostjo (1,87 %). Izračune so ovrednotili in potrdili z eksperimentalnimi preizkusi izdelave prevlek z majhno poroznostjo, ki so jih izdelali z izbranim HVAF postopkom pri izračunani optimalni razdalji napršev anja.

Ključne besede: amorfna prevleka na osnovi Ni, postopek napršev anja v mešanici propana in zraka (HVAF), računalniška simulacija, razdalja napršev anja

1 INTRODUCTION

Because of their high glass-transition temperature and excellent corrosion resistance, Ni-based amorphous alloys show ultra-high strength and high thermal stability.[1] Generally, Ni-based amorphous alloys are made into thin strips, powders and wires with small diameters. Therefore, the glass-forming ability limits the use of amorphous alloys as structural materials. However, amorphous coatings based on Ni-based metallic glass systems prepared on a substrate with different methods can overcome this drawback.

Nowadays, there are several methods used for producing amorphous coatings, such as the laser cladding and thermal spray-based techniques. It is reported that Ni-based amorphous alloy coatings were successfully applied onto metal parts, and these coatings have the best corrosion resistance compared with the properties of crystalline substrates.[2,3] In laser cladding, coatings are typically complex structures composed of amorphous, nanocrystalline and metal compound phases. Amorphous powder is completely melted by laser cladding, and then cooled down and solidified to form a coating. However, the amorphous content in a coating is extremely rare, and the thermal stress and residual stress in the coating can easily lead to cracking during rapid cooling.[4,5] In addition, some amorphous metal coatings were prepared within a Ni-based alloy system, mainly through plasma spraying and high-velocity oxygen fuel (HVOF) spraying.[6,7] HVAF and HVOF are similar spraying processes, but the difference is that in the former air is used instead of oxygen. Considering that high-speed particles can produce dense coatings,[8] HVAF is a good candidate for preparing Ni-based amorphous alloy coatings. However, fully amorphous Ni-based coatings have been difficult to achieve with HVAF so far.

Porosity is one of the most important parameters for determining the quality of thermal sprayed coatings, because it can significantly affect mechanical and chemical magnetism and thermal conductivity, and has a signifi-

*Corresponding author's e-mail:
wunianchu@163.com (Nianchu Wu)

cant impact on the conductivity of a coating material.[9–11] The velocity and temperature of particles colliding with the substrate affect the structure of the deposit, which strongly affects the porosity of an HVOF sprayed coating.[12,13] Many numerical and experimental studies show that the spraying distance is also related to the particle velocity and temperature.[14,15] Therefore, spraying distance is an important parameter that affects the final porosity of HVOF thermal sprayed coatings.[16] We can optimize the spraying distance through repeated experiments. Although this method is expensive, it is reliable. The effect of spraying distance on the porosity of an HVOF thermal sprayed WC-12 % Co coating was studied using a numerical computational fluid dynamics (CFD) simulation.[15] The speed and temperature of small particles depend on the spraying distance. However, there are few experiments about the effect of the spraying distance on the porosity of HVAF sprayed Ni-based AMCs. Therefore, it is very important to study the relationship between the spraying distance and coating porosity during HVAF spraying of Ni-based AMCs by combining the CFD simulation and experiments.

In our study, an $Ni_{53}Nb_{20}Ti_{10}Zr_8Co_6Cu_3$ (at.%) amorphous alloy is used as the thermal spraying material because this alloy exhibits an excellent glass-forming ability.[17] Through a CFD simulation, the effect of injection distance on the characteristics of Ni-based amorphous particles during injection was studied. Using the best spraying distance predicted by the simulation, Ni-based AMCs with low porosity were prepared with HVAF thermal spraying.

2 MATHEMATICAL MODELING

2.1 HVAF thermal spray gun model and the boundary

Figure 1 shows the detailed grid of the AK06 spray gun. The numerical methods and mathematical models are applied to a propane-fueled 2-D geometry. There are 82331 units and 83235 nodes in the whole domain. The grids around the free jet area, the air-fuel inlet and the nozzle have been successively refined to accurately capture the characteristics of the flame flow. **Table 1** shows the spray parameters for HVAF sprayed Ni-based AMCs. The distance between the base plate and the nozzle outlet is (300, 350 and 400) mm, respectively. We use a carrier gas to introduce powder particles downstream of the nozzle.[18] The variation range of the particles injected into the nozzle is 15–55 μm. The other parameters are set, assuming that the inlet temperatures of both the propane-air inlet and the particle inlet are 300 K, and that the wall of the spray gun is at a constant temperature of 300 K. The pressure far field and pressure outlet boundaries should be applied to the external area. Finally, the atmospheric pressure is set to 1.01 KPa.

Table 1: HVAF spray parameters for Ni-based AMCs

air pressure (Psi)	propane pressure (Psi)	nitrogen pressure (Psi)	chamber pressure (Psi)	feed rate (g/min)	traverse velocity (mm/s)	spray distance (mm)
90.4	94.8	76.0	74.3	30	500	300
90.4	94.8	76.0	74.3	30	500	350
90.4	94.8	76.0	74.3	30	500	400

2.2 Gas flow model

The "realizable k-ε model" is widely used in the HVAF simulation. The governing equations for the 2-D model in a Cartesian tensor are defined below:[19]

Mass conservation equation:

$$\frac{\partial \rho}{\partial t} + \frac{\partial}{\partial x_i}(\rho u_i) = 0 \tag{1}$$

Momentum conservation:

$$\frac{\partial}{\partial t}(\rho u_i) + \frac{\partial}{\partial x_j}(\rho u_i u_j) = \\ = \frac{\partial p}{\partial x_i} + \frac{\partial}{\partial x_j}(\tau_{ij})_{\text{eff}} + \frac{\partial}{\partial x_j}(-\rho \vec{u}_i \vec{u}_j) \tag{2}$$

Energy transport equation:

$$\frac{\partial}{\partial t}(\rho E) + \frac{\partial}{\partial x_i}\left[u_i(\rho E + p)\right] = \\ = \frac{\partial}{\partial x_j}\left(k_{\text{eff}}\frac{\partial T}{\partial x_j} + u_i(\tau_{ij})_{\text{eff}}\right) + S_{\text{h}} \tag{3}$$

$$(\tau_{ij})_{\text{eff}} = \mu_{\text{eff}}\left(\frac{\partial u_j}{\partial x_i} + \frac{\partial u_i}{\partial x_j}\right) - \frac{2}{3}\mu_{\text{eff}}\frac{\partial u_i}{\partial x_i}\rho_{ij} \tag{4}$$

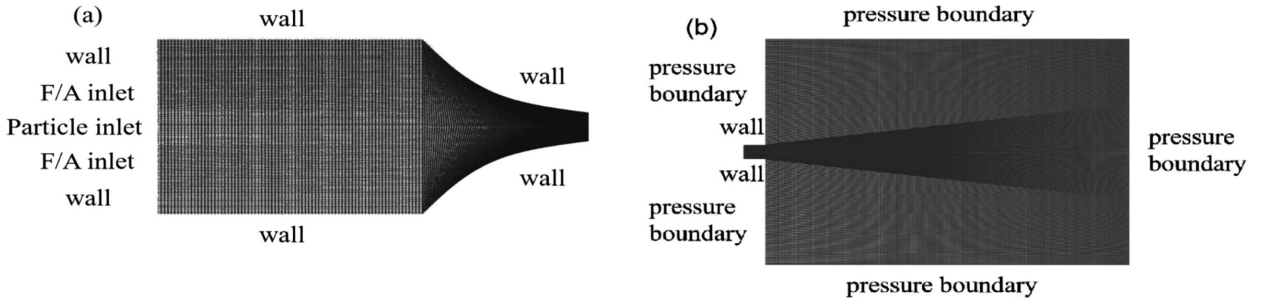

Figure 1: Computational grid and boundary conditions used in the HVAF model: a) internal domain, including the combustion chamber and the convergent-divergent nozzle, b) external domain

where the effective thermal conductivity is:

$$k_{\text{eff}} = k + \frac{c_{\text{p}} \mu_{\text{t}}}{\rho_t} \tag{5}$$

2.3 Combustion model

There are complex chemical reactions between hydrocarbons and air in an HVAF chamber. They include a large number of basic reactions, and the atoms have strong thermal vibrations. The combustion products may decompose due to a high temperature and high pressure.[20] Therefore, it is necessary to simplify the complex combustion chamber reaction. In this study, a stoichiometric calculation of each product was completed using the chemical balance code developed by Gordon and McBride. The chemical reactions in our model are as follows:

$$\begin{aligned} &C_3H_8+4.762O_2+0.014N_2 \rightarrow 0.47CO+2.553CO_2+ \\ &+0.009H+0.129H_2+3.843H_2O+0.027NO+0.002O+ \\ &0.037OH+0.026O_2 \end{aligned} \tag{6}$$

The eddy dissipation model is applied to the reaction. This approach is based on the solution of the transport equations for species mass fractions. It is assumed that the turbulence controls the reaction rate rather than the calculation of the Arrhenius chemical kinetics. The net rate of production for species *i* due to reaction *r* is given by the smaller of the two equations below:

$$R_{i,\text{r}} = v_{i,\text{r}} M_{\text{w},i} A \rho \frac{\varepsilon}{k} \min\left(\frac{Y_{\text{R}}}{v_{\text{R,r}} M_{\text{w,R}}} \right) \tag{7}$$

$$R_{i,\text{r}} = v_{i,\text{r}} M_{\text{w},i} AB \rho \frac{\varepsilon}{k} \min\left(\frac{\sum_{\text{P}} Y_{\text{P}}}{\sum_{j}^{N} v_{j,\text{r}} M_{\text{w,R}}} \right) \tag{8}$$

2.4 Particle models

Using the Navier-Stokes equation, the gas is considered as the continuous phase, and the dispersed particle phase is solved by tracking a large number of liquid droplets. In addition to calculating the heat and mass transfer to the gas phase, the trajectories of these discrete phase entities are also calculated.

When Cartesian coordinates are used, the motion equation of the particles in the x direction can be written as the force balance, and the inertia of liquid droplets is equal to the force acting on the particles. The basic equation of particles is as follows:[18]

$$\frac{\text{d}u_{\text{p}}}{\text{d}t} = \frac{18\mu}{\rho_{\text{p}} d_{\text{p}}^2} \frac{C_{\text{D}} \text{Re}}{24} (u - u_{\text{p}}) + F_x$$

The following formula is the energy equation for a single particle, ignoring the radiation heat transfer:[21]

$$m_{\text{p}} C_{\text{p}} \frac{\text{d}T_{\text{p}}}{\text{d}t} = hA_{\text{p}} (T_{\text{g}} - T_{\text{p}})$$

where the material characteristic parameters of the Ni-based amorphous powders used in this study are as follows: ρ_p = 8200 kg/m^3 and c_p = 400 J/(kg·K).

3 EXPERIMENTAL PROCEDURE

The material used in this work is an $Ni_{53}Nb_{20}Ti_{10}Zr_8Co_6Cu_3$ (at. %) alloy. It is prepared by melting an appropriate amount of high-purity elements in a water-cooled copper crucible in an argon atmosphere with titanium absorption by an electric arc. Amorphous ribbons were fabricated using a Bühler melt spinner (Hechingen, Germany) and the copper wheel was rotating at a speed of 40 m/s. After heating to about 1473 K with a tightly coupled annular nozzle, the amorphous powder is prepared by the atomization of high-purity argon under a dynamic pressure of 7 MPa, with a size of 15–55 μm. Atomized powders are screened based on a traditional sieve analysis and divided into different particle size ranges. We select (100 × 40 × 5) mm 304 type stainless steel plate as the base. The $Ni_{53}Nb_{20}Ti_{10}Zr_8Co_6Cu_3$ AMC is prepared using the AK07 HVAF thermal spraying system by Kermetico. Table 1 shows detailed spraying parameters of the HVAF process.

The microstructures of the powder and coating can be detected with scanning electron microscopy (Quanta 600). The band and coating are analyzed with X-ray diffraction (XRD) with a monochromatic Cu-K_α radiation (k = 0.1542 nm) on a Rigaku D/max 2400 diffractometer (Tokyo, Japan). Due to its simplicity, accessibility and ability to measure porosity, the image analysis technology has become a popular method to determine the porosity of thermal sprayed coatings.[22,23] There is a high contrast between dark holes and coating material with high reflectivity so that porosity can be clearly detected in SEM micrographs by analyzing the images. They are analyzed using Image Pro Plus 6.0 software to evaluate the porosity. To ensure data accuracy, 20 random and non-overlapping SEM image fields are taken for each sample. All images are taken under the same parameters (such as acceleration voltage, working distance, resolution and magnification).

4 RESULTS AND DISCUSSION

4.1 Gas dynamics for different spray distances

Figures 2 and **3** show the relationship between different injection distances (300, 350, 400) mm and the predicted pressure, gas temperature and gas velocity of the flame along the centerline. When air and propane are transported to the combustion chamber, a chemical reaction occurs between the two substances, which converts them into high-temperature and high-pressure gases. The generation of a supersonic flame flow is inseparable from the flow of the high-pressure gas through a restricted nozzle. The gas pressure in the combustion

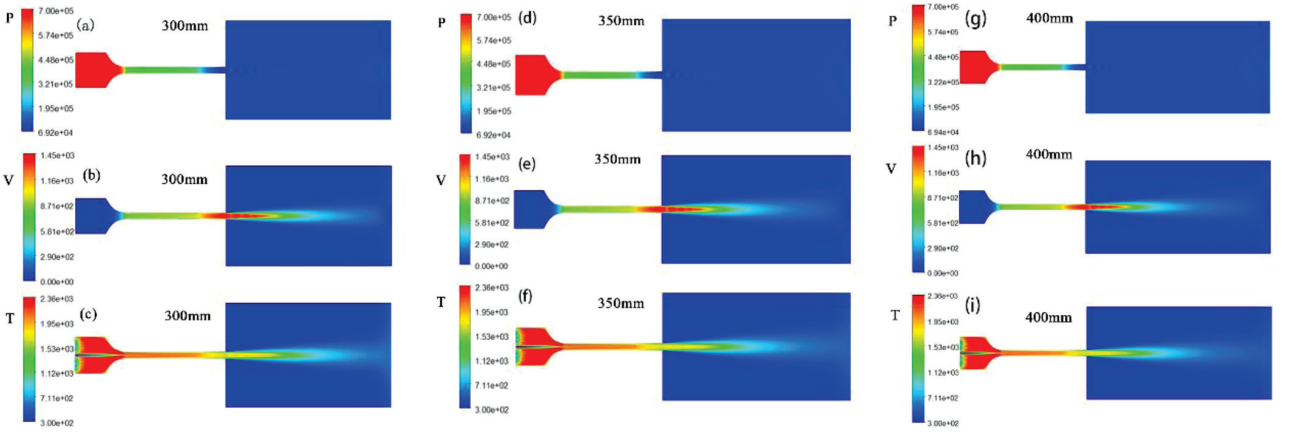

Figure 2: a), d), g) Contours of gas pressure, b), e), h) gas temperature and c), f), i) gas velocity magnitude for different spray distances (300, 350, 400) mm

chamber is about 7 KPa, and the pressure in the barrel is less than 1.0 KPa; the pressure fluctuation near the gun outlet is shown in **Figures 2a**, **2d** and **2g** and **Figures 3a**, **3d** and **3g**. The fluctuation of the flame pressure at the nozzle outlet is caused by a periodic over-expansion of the air flow and subsequent re-concentration above and below the atmospheric pressure.[24]

In general, (**Figures 2b**, **2e** and **2h** and **Figures 3b**, **3e** and **3h**) the gas temperature in the combustion nozzle and chamber rises sharply and reaches a peak near the nozzle outlet. Notably, the higher centerline temperature is about 2000 K. On the outside of the spray gun, the effect of the spray distance on the temperature is zero. **Figures 2c**, **2f** and **2i** and **Figures 3c**, **3f** and **3i** show the

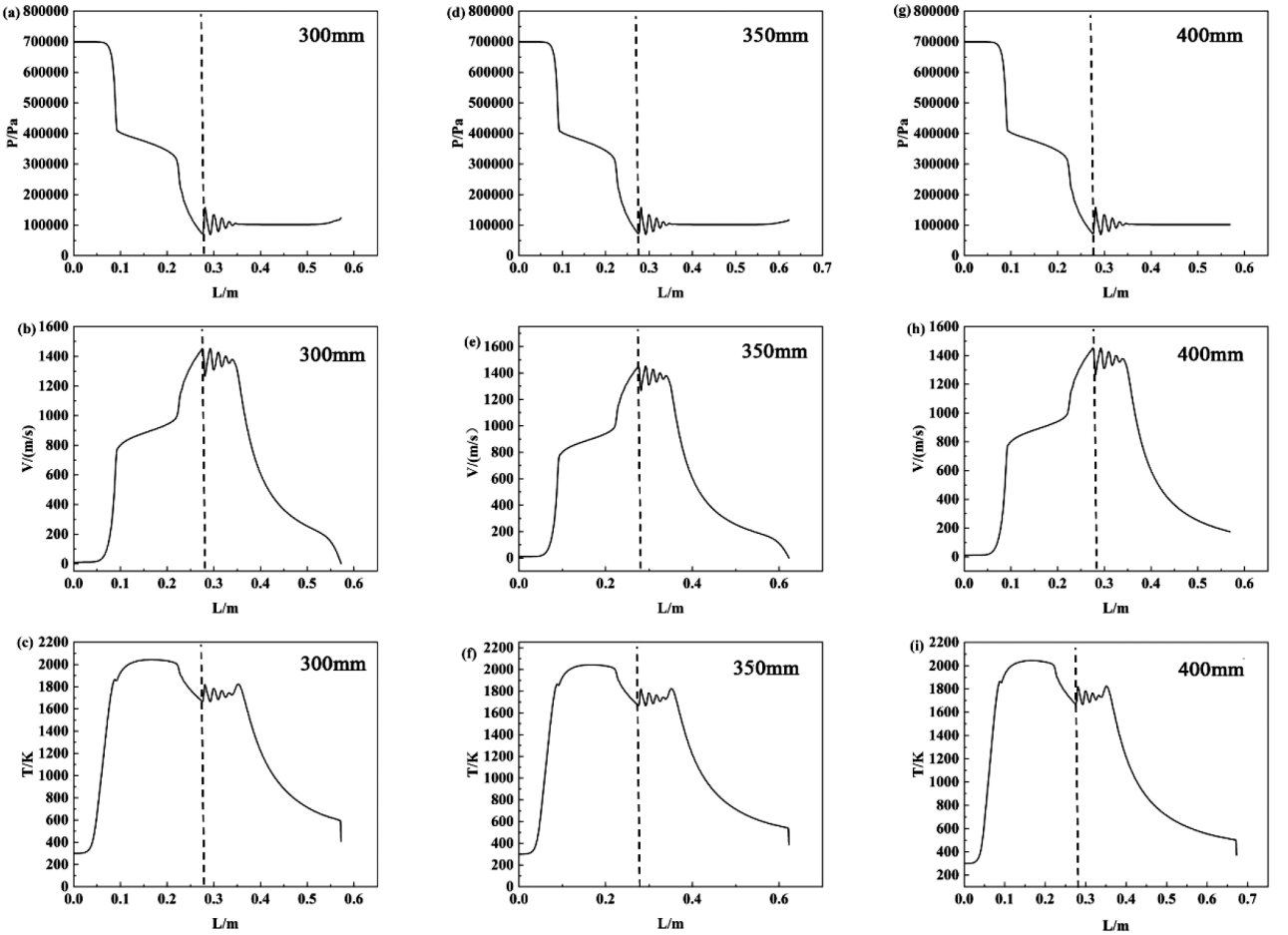

Figure 3: Calculated contours of the flame and gas characteristics along the centerline: a), d), g) gas pressure (Pa), b), e), h) gas temperature (K), c), f), i) gas velocity magnitude (m/s) at different spray distances (300, 350, 400) mm

centerline axial gas velocities plotted against the axial distance. The speed variation trend in the C-D nozzle and cylinder is gradually increasing. At the nozzle outlet, due to the spiral of the expansion compression wave outside the nozzle, the expansion compression wave velocity presents a sharp increase trend, and then it decreases. After five diamond impacts, the ambient air slows down as it reaches the centerline.

4.2 Effect of the spray distance on the particle velocity and temperature

Figures 4a, **4c** and **4e** show the function of particle velocity as a function of distance along the centerline when the spray distance varies (300, 350, 400) mm. According to the experimental data, the particle size has a significant impact on the acceleration and deceleration behavior of particles. Small-sized particles (15 μm) can reach a very high speed (nearly 700 m/s) during flight. However, as their momentum inertia is small, the speed of small particles is much lower than that of large particles. The acceleration of larger particles is slower, and they can reach their maximum speed when they hit the substrate. The axial velocity of particles as a function of the particle size is shown in **Figure 4g**. As shown in the figure, the smaller the particle size, the faster is its speed.

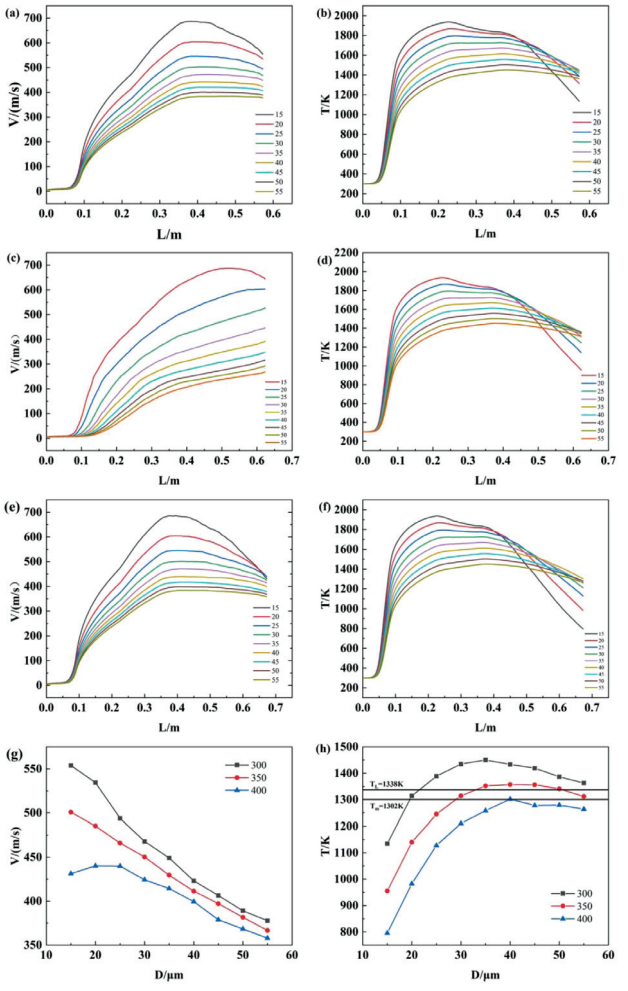

Figure 4: Effect of spray distance (300, 350, 400) mm on: a), c), e) particle velocity and b), d), f) particle temperature for a particle size of 15–55 μm, g) predicted particle axial velocity and h) temperature at spray distances of (300, 350, 400) mm for the particle size of 15–55 μm

Figures 4b, **4d** and **4f** show the predicted temperature of the particles with nine different diameters at the jet's centerline for different spray distances (300, 350, 400) mm. Small-sized particles (15 μm) take a short time to heat to the melting point, and they can completely melt during flight. However, after a long flight, they may eventually be in a liquid-solid coexistence state, or even completely in a solid state. For small particles, it is extremely easy to change their temperature due to their small thermal inertia. For large-sized particles e.g. (45, 50, 55) μm, the acceleration and heating time are longer, and their temperature distribution becomes almost average.

Figures 4g and **4h** show the axial particle velocity and temperature at spray distances of (300, 350 and 400) mm for the particle size of 15–55 μm. It can be seen that the axial particle velocity and temperature at impact increase with the spray distance for the particle size of 15–55 μm. Due to a short spray distance, particles of several microns can be completely melted. The spray distance is short, and even particles of a few microns can melt completely. However, as the spray distance increases, they do not melt completely, but they partially melt, or even remain solid when impinging on the substrate, as they solidify due to the effect of temperature decay on the free jet. Typically, the change in the spray distance affects small particles (less than 30 μm), and the impact on large particles is greater than that on small particles. This is because with a rapid increase in the spray distance, the velocity and temperature of small particles impacting the substrate significantly decrease. However, the velocity and temperature of large particles decrease slowly as the spray distance increases.

The two most important factors that determine the porosity of HVAF coatings are the particle velocity and temperature.[25,26] The change in the particle velocity is usually related to the improvement of splash deformation, but has little effect on porosity. The melting behavior of particles depends on the particle temperature, which is the key for a low porosity and dense coating.[27,28] When the temperature of the powder is between the solidus temperature and liquidus temperature (T_m and T_L) of the Ni-based amorphous material, the best thermal spraying effect is obtained. At the spray distance of 350 mm, particles mostly melt during flight because their temperature is between T_m = 1302 K and T_L = 1338 K, as shown in **Figure 4h**. Thus, the computational results of this work show that the optimal spray distance is 350 mm for the Ni-based AMCs.[29]

4.3 Experimental validation

The Ni-based AMCs were prepared using the powder with three spray distances (350, 400, 450) mm to verify the simulation results. **Figure 5** shows a SEM image of the $Ni_{53}Nb_{20}Ti_{10}Zr_8Co_6Cu_3$ feedstock powder. In an argon environment, most particles produced with gas atomization are spherical or near-spherical. Although some particles are attached to small satellites, most particles have a smooth surface and good fluidity. **Figure 6** shows the XRD patterns of the deposited coating of atomized powder, $Ni_{53}Nb_{20}Ti_{10}Zr_8Co_6Cu_3$ melt-spun ribbon and spray powder of various particle sizes. The diffusion mode and an absence of any peak related to the crystalline phase indicate that they are completely amorphous.

Figure 7 shows the cross-sectional structures and surface morphologies of different Ni-based AMCs. In **Figure 7c**, the surface morphology shows that at the spraying distance of 400 mm the coating is not completely melted during the spraying process. In **Figure 7a**, the surface morphology of the coating applied at the spraying distance of 300 mm shows that the coating is completely melted. Therefore, at the spraying distance of 350 mm, an almost completely dense coating is obtained (**Figure 7d**), with a porosity as low as 1.87 %. As the spraying distance increases, the porosity of the coating increases to 3.50 % with the spraying distance of 300 mm (**Figure 7e**) and it is as high as 4.96 % when the spraying distance is 400 mm (**Figure 7f**). These results imply that the porosity of an HVAF coating is largely dependent on the spraying distance and that the densest coating can be obtained using the spraying distance of 350 mm.

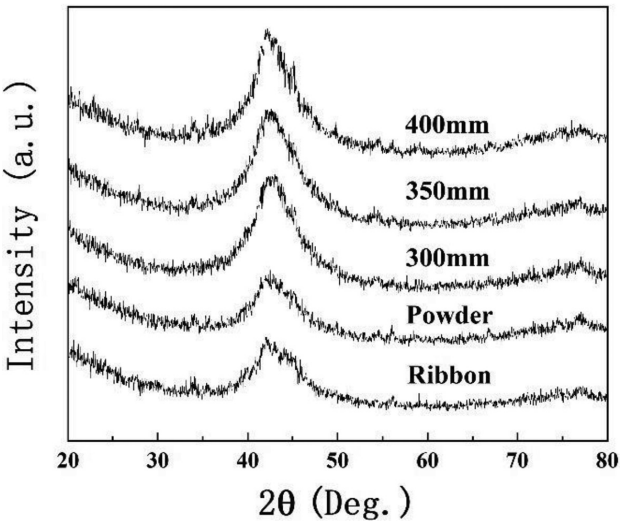

Figure 6: XRD patterns for different $Ni_{53}Nb_{20}Ti_{10}Zr_8Co_6Cu_3$ distances (300, 350, 400 mm)

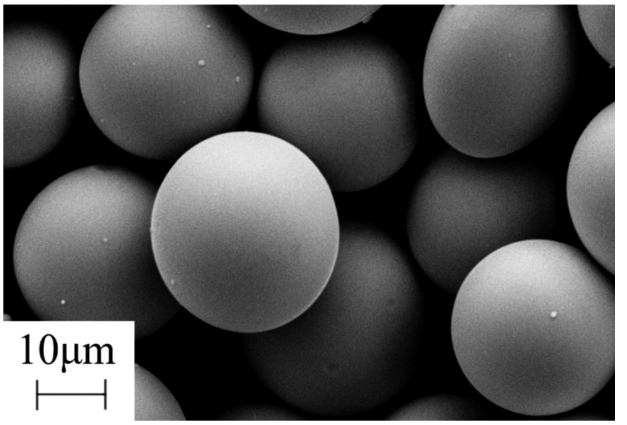

Figure 5: SEM image of $Ni_{53}Nb_{20}Ti_{10}Zr_8Co_6Cu_3$ alloy powder

5 CONCLUSIONS

The effect of the spraying distance on the porosity of Ni-based AMCs during HVAF thermal spraying was studied by means of a predictive simulation, and was

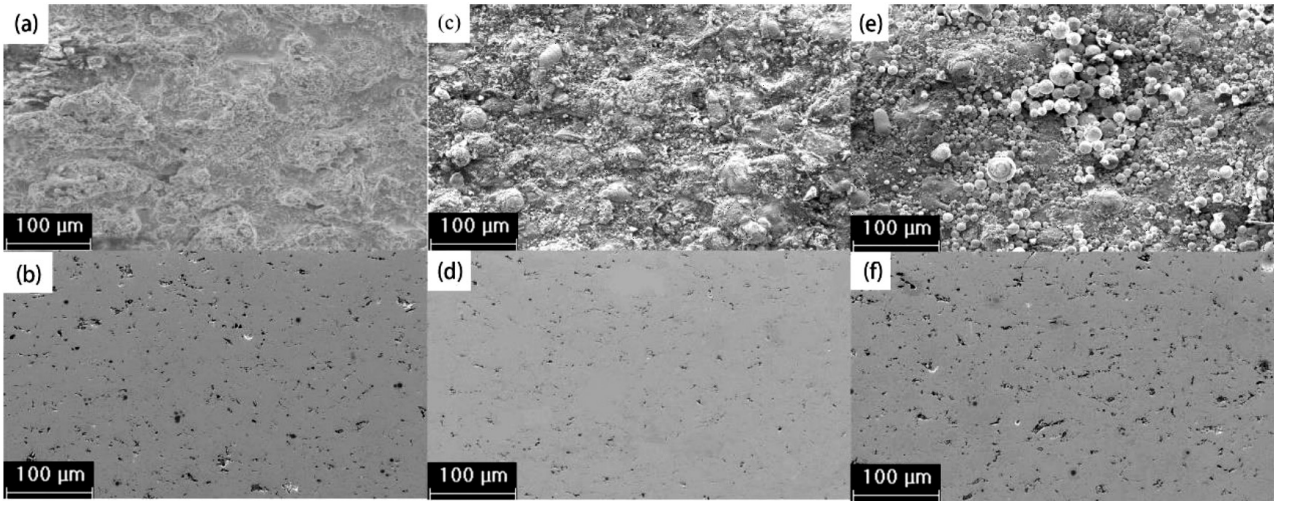

Figure 7: a), c), e) SEM micrographs of the as-sprayed surfaces and b), d), f) cross-sections show the general characteristics of the three HVAF coatings made from different spray distances (300, 350, 400) mm

verified with experiments. The flight behavior of Ni-based amorphous alloy powder particles during HVAF spraying was studied using computational fluid dynamics (CFD). According to the prediction results, the static pressure of combustion products in the combustion chamber can reach 7 KPa, and the flame temperature can reach 2000 K. The particle size strongly affects the temperature and velocity of the particles. Spraying distance significantly affects the particles with a size of less than 30 μm, changing their velocity and temperature. When the temperature of the powder is kept between the solidus and liquidus temperatures of the Ni-based amorphous alloy, the optimal thermal spraying distance is 350 mm. Using this optimized spraying distance, we obtained a low-porosity Ni-based AMC.

Notation

A_p surface area of the particle
C_D drag coefficient
c_p specific heat of the particle
d_p particle diameter
E enthalpy
F_x additional acceleration
h heat transfer coefficient
k thermal conductivity
k_{eff} effective thermal conductivity
m_p mass of the particle
Re Reynolds number
S_h chemical reaction source energy
T temperature
T_g gas temperature
T_p particle temperature
u velocity
u_i velocity in the i-direction
u_p particle velocity
x_i coordinate in the i-direction
A constant in eddy dissipation model = 4.0
B constant in eddy dissipation model = 0.5
k kinetic energy, m^2/s^2
$M_{w,i}$ molecular weight of species i
$M_{\omega,R}$ molecular weight of reactant R
$M_{\omega j}$ molecular weight of reactant j
N number of chemical species in the system
p pressure, Pa
$R_{i,r}$ net rate of production of species i due to reaction r
$v_{i,r}$ stoichiometric coefficient for reactant i in reaction r
Y_P mass fraction of product P
Y_R mass fraction of a particular reactant, R

Greek letters

δ Kronecker symbol
μ viscosity
μ_t turbulent viscosity
ρ density
τ deviatoric stress tensor

Subscripts

g gas
i,j coordinate indices
p particle
ε turbulence dissipation rate, m^2/s^3

Acknowledgements

This work was supported by the Educational Commission of the Liaoning Province of China under Grant No. L2020021, Natural Science Foundation of the Liaoning Province under Grant No. 2022-MS-364 and Fushun Revitalization Talents Program under Grant No. FSYC202107011.

6 REFERENCES

[1] A. Inoue, W. Zhang, T. Zhang, Thermal stability and mechanical strength of bulk glassy Ni-Nb-Ti-Zr alloys, Mater. Trans., 43 (**2002**) 8, 1952–1956, doi:10.2320/matertrans.43.1952

[2] A. P. Wang, X. C. Chang, W. L. Hou, J. Q. Wang, Preparation and corrosion behaviour of amorphous Ni-based alloy coatings, Mater. Sci. Eng., 449 (**2007**), 277–280, doi:10.1016/j.msea.2006.02.366

[3] A. P. Wang, T. Zhang, J. Q. Wang, Ni-based fully amorphous metallic coating with high corrosion resistance, Philos. Mag. Lett., 86 (**2006**) 1, 5–11, doi:10.1080/09500830500479718

[4] Y. Z. Lu, G. K. Huang, Y. Z. Wang, H. G. Li, Z. X. Qin, X. Lu, Crack-free Fe-based amorphous coating synthesized by laser cladding, Mater. Lett., 210 (**2018**), 46–50, doi:10.1016/j.matlet.2017.08.125

[5] Y. X. Chew, J. H. L. Pang, G. J. Bi, B. Song, Thermo-mechanical model for simulating laser cladding induced residual stresses with single and multiple clad beads, J. Mater. Process. Technol., 224 (**2015**), 89–101, doi:10.1016/j.jmatprotec.2015.04.031

[6] A. H. Dent, A. J. Horlock, D. G. Mccartney, S. J. Harris, Microstructural characterisation of a Ni-Cr-B-C based alloy coating produced by high velocity oxy-fuel thermal spraying, Surf. Coat. Technol., 139 (**2001**) 2–3, 244–250, doi:10.1016/S0257-8972(01)00996-3

[7] H. Choi, S. Yoon, G. Kim, H. Jo, C. Lee, Phase evolutions of bulk amorphous NiTiZrSiSn feedstock during thermal and kinetic spraying processes, Scr. Mater., 53 (**2005**) 1, 125–130, doi:10.1016/j.scriptamat.2005.01.046

[8] Y. Wang, Z. Z. Xing, Q. Luo, A. Rahmam, J. Jiao, S. J. Qu, Y. G. Zheng, J. Shen, Corrosion and erosion-corrosion behaviour of activated combustion high-velocity air fuel sprayed Fe-based amorphous coatings in chloride-containing solutions, Corros. Sci., 98 (**2015**), 339–353, doi:10.1016/j.corsci.2015.05.044

[9] C. Zhang, R. Q. Guo, Y. Yang, Y. Wu, L. Liu, Influence of the size of spraying powders on the microstructure and corrosion resistance of Fe-based amorphous coating, Electrochim. Acta, 56 (**2011**) 18, 6380–6388, doi:10.1016/j.electacta.2011.05.020

[10] L. Qiao, Y. P. Wu, S. Hong, J. Cheng, Z. Wei, Influence of the high-velocity oxygen-fuel spray parameters on the porosity and corrosion resistance of iron-based amorphous coatings, Surf. Coat. Technol., 366 (**2019**), 296–302, doi:10.1016/j.surfcoat.2019.03.046

[11] N. C. Wu, K. Chen, W. H. Sun, J. Q. Wang, Correlation between particle size and porosity of Fe-based amorphous coating, Surf. Eng., 35 (**2019**) 1, 37–45, doi:10.1080/02670844.2018.1447782

[12] J. He, M. Ice, E. Lavernia, Particle melting behavior during high-velocity oxygen fuel thermal spraying, J. Therm. Spray Technol., 10 (**2001**), 83–93, doi:10.1361/105996301770349547

[13] T. C. Hanson, G. S. Settles, Particle temperature and velocity effects on the porosity and oxidation of an HVOF corrosion-control coating,

J. Therm. Spray Technol., 12 (**2003**), 403–415, doi:10.1361/105996303770348276

[14] E. Dongmo, M. Wenzelburger, R. Gadow, Analysis and optimization of the HVOF process by combined experimental and numerical approaches, Surf. Coat. Technol., 202 (**2008**) 18, 4470–4478, doi:10.1016/j.surfcoat.2008.04.029

[15] M. H. Li, P. D. Christofides, Multi-scale modeling and analysis of an industrial HVOF thermal spray process, Chem. Eng. Sci., 60 (**2005**) 13, 3649–3669, doi:10.1016/j.ces.2005.02.043

[16] K. Murugan, A. Ragupathy, V. Balasubramanian, K. Sridhar, Optimizing HVOF spray process parameters to attain minimum porosity and maximum hardness in WC-10Co-4Cr coatings, Surf. Coat. Technol., 247 (**2014**), 90–102, doi:10.1016/j.surfcoat.2014.03.022

[17] M. H. Lee, J. Y. Lee, D. H. Bae, W. T. Kim, D. J. Sordelet, D. H. Kim, A development of Ni-based alloys with enhanced plasticity, Intermetallics, 12 (**2004**) 10–11, 1133–1137, doi:10.1016/j.intermet.2004.04.027

[18] H. Tabbara, S. Gu, Computational simulation of liquid-fuelled HVOF thermal spraying, Surf. Coat. Technol., 204 (**2009**) 5, 676–684, doi:10.1016/j.surfcoat.2009.09.005

[19] S. Kamnis, S. Gu, Numerical modelling of propane combustion in a high velocity oxygen-fuel thermal spray gun, Chem. Eng. Process.: Process Intensif., 45 (**2006**) 4, 246–253, doi:10.1016/j.cep.2005.06.011

[20] D. Cheng, Q. Xu, G. Tapaga, E. J. Lavernia, A numerical study of high-velocity oxygen fuel thermal spraying process. Part I: Gas phase dynamics, Metall. Mater. Trans. A., 32 (**2001**), 1609–1620, doi:10.1007/s11661-001-0139-1

[21] M. H. Khan, T. Shamim, Investigation of a dual-stage high velocity oxygen fuel thermal spray system, Appl. Energy, 130 (**2014**), 853–862, doi:10.1016/j.apenergy.2014.03.075

[22] G. Montavon, C. Coddet, C. C. Berndt, S. H. Leigh, Microstructural index to quantify thermal spray deposit microstructures using image analysis, J. Therm. Spray Technol., 7 (**1998**), 229–241, doi:10.1361/105996398770350972

[23] S. Deshpande, A. Kulkarni, S. Sampath, H. Herman, Application of image analysis for characterization of porosity in thermal spray coatings and correlation with small angle neutron scattering, Surf. Coat. Technol., 187 (**2004**) 1, 6–16, doi:10.1016/j.surfcoat.2004.01.032

[24] H. Tabbra, S. Gu, A study of liquid droplet disintegration for the development of nanostructured coatings, AIChE J., 58 (**2012**) 11, 3533–3544, doi:10.1002/aic.13755

[25] R. Ghafouri-Azar, J. Mostaghimi, S. Chandra, M. Charmchi, A stochastic model to simulate the formation of a thermal spray coating, J. Therm. Spray Technol., 12 (**2003**), 53–69, doi:10.1361/105996303770348500

[26] J. J. Pan, S. S. Hu, L. J. Yang, K. Y. Ding, B. Q. Ma, Numerical analysis of flame and particle behavior in an HVOF thermal spray process, Mater. Des., 96 (**2016**), 370–376, doi:10.1016/j.matdes.2016.02.008

[27] J. Mostaghimi, S. Chandra, R. Ghafouri-Azar, A. Dolatabadi, Modeling thermal spray coating processes: a powerful tool in design and optimization, Surf. Coat. Technol., 163 (**2003**), 1–11, doi:10.1016/s0257-8972(02)00686-2

[28] J. A. Hearley, J. A. Little, A. J. Sturgeon, The effect of spray parameters on the properties of high velocity oxy-fuel NiAl intermetallic coatings, Surf. Coat. Technol., 123 (**2000**) 2–3, 210–218, doi:10.1016/S0257-8972(99)00511-3

[29] G. H. Dai, J. Sang, Y. F. Wang, Research Progress of Natural Gas Dehydration with Supersonic Separator, J. Petrochem. Univ., 34 (**2021**) 1, 63–71, doi:10.3969/j.issn.1006-396X.2021.01.011